

AGILE: Hand-Object Interaction Reconstruction from Video via Agentic Generation

Jin-Chuan Shi^{1*} Binhong Ye^{1*} Tao Liu¹ Junzhe He¹ Yangjinhui Xu¹ Xiaoyang Liu¹
Zeju Li¹ Hao Chen¹ Chunhua Shen^{1,2}

¹ State Key Lab of CAD & CG, Zhejiang University ² Zhejiang University of Technology



Figure 1. **High-Fidelity Hand-Object Reconstruction from Video.** We present AGILE, a framework that reconstructs simulation-ready interaction sequences from monocular video. By leveraging agentic generative priors, AGILE robustly recovers watertight geometry, realistic textures, and precise 6D poses for diverse objects, ranging from thin structures (scissors, pen) to complex topologies (game controller), even under severe hand occlusion and rapid manipulation.

Abstract

Reconstructing dynamic hand-object interactions from monocular videos is critical for dexterous manipulation data collection and creating realistic digital twins for robotics and VR. However, current methods face two prohibitive barriers: (1) reliance on neural rendering often yields fragmented, non-simulation-ready geometries under heavy occlusion, and (2) dependence on brittle Structure-from-Motion (SfM) initialization leads to frequent failures on in-the-wild footage. To overcome these limitations, we introduce AGILE, a robust framework that shifts the paradigm from reconstruction to agentic generation for interaction learning. First, we employ an agentic pipeline where a Vision-Language Model (VLM) guides a genera-

tive model to synthesize a complete, watertight object mesh with high-fidelity texture, independent of video occlusions. Second, bypassing fragile SfM entirely, we propose a robust anchor-and-track strategy. We initialize the object pose at a single interaction onset frame using a foundation model and propagate it temporally by leveraging the strong visual similarity between our generated asset and video observations. Finally, a contact-aware optimization integrates semantic, geometric, and interaction stability constraints to enforce physical plausibility. Extensive experiments on HO3D, DexYCB, and in-the-wild videos reveal that AGILE outperforms baselines in global geometric accuracy while demonstrating exceptional robustness on challenging sequences where prior arts frequently collapse. By prioritizing physical validity, our method produces simulation-ready assets validated via real-to-sim retargeting for robotic applications. Project page: <https://agile-hoi.github.io>.

* Equal contribution.

1. Introduction

Reconstructing dynamic hand-object interactions (HOI) from monocular video is a pivotal challenge in computer vision and graphics. The ultimate aspiration is to create high-fidelity digital twins of these interactions, assets that are not only visually coherent but also geometrically explicit and physically plausible for downstream tasks such as robotic imitation learning and physics-based simulation. While the internet offers a vast repository of in-the-wild interaction videos, converting this data into simulation-ready 3D assets remains an unresolved challenge. We identify two fundamental barriers in existing pipelines that hinder scalability and reliability.

The first barrier lies in the inherent limitations of *reconstruction-based geometry*. State-of-the-art methods typically rely on neural rendering techniques, such as NeRF [15] or 3D Gaussian Splatting [10], to optimize scene representations [7, 16]. However, these methods fundamentally depend on multi-view consistency. In HOI scenarios, severe hand occlusion frequently violates this premise, leading to fragmented, noisy, or non-watertight geometries. Such representations, while visually passable from trained viewpoints, are ill-suited for physics engines that require clean, explicit topology.

The second, and more critical, bottleneck is the *brittleness of pose initialization*. Most prevailing approaches [7, 31] are anchored on Structure-from-Motion (SfM) pipelines like COLMAP [23] to estimate initial camera and object poses. SfM is notoriously fragile in dynamic scenes featuring textureless objects, rapid motions, or significant occlusions. When SfM fails to register frames, a common occurrence in real-world footage, the entire pipeline collapses. This reliance on classic geometric matching prevents current methods from achieving reliable performance on complex benchmarks [2].

Recent generative advancements offer potential but lack robustness for high-fidelity HOI. MagicHOI [31] leverages diffusion priors but produces over-smoothed meshes and retains a dependency on brittle SfM. Single-view methods like SAM3D [26] suffer from occlusion-induced information loss, yielding coarse geometries and poor textures that destabilize subsequent pose optimization. To overcome these barriers, it is essential to aggregate multi-view cues from the video. However, since standard 3D generators require canonical cameras unavailable in dynamic footage, we must resort to 2D generative priors to synthesize missing perspectives. Yet, the stochastic nature of 2D diffusion models frequently introduces hallucinations inconsistent with the actual object in the video. Consequently, reliably harnessing these priors requires an intelligent mechanism capable of identifying informative frames and strictly filtering generated views for consistency—a capability missing in current end-to-end pipelines.

To bridge this gap, we introduce AGILE, a robust framework that shifts the paradigm from *reconstruction* to *agenetic generation* for interaction learning. First, we employ an agentic pipeline where a Vision-Language Model (VLM) acts as an intelligent supervisor. The VLM selects informative keyframes to guide multi-view synthesis and rigorously filters the outputs via rejection sampling to ensure consistency. Crucially, the pipeline incorporates a *texture refinement* phase that recovers high-frequency details from the video observations. This yields a watertight mesh with hyper-realistic appearance—a prerequisite that enables our subsequent foundation models to reliably initialize pose and optimize semantic alignment.

Leveraging this high-quality asset, we propose a robust *anchor-and-track* optimization strategy that eliminates the need for brittle SfM. We utilize a foundation model to initialize the object pose only at a single interaction onset frame. For the remainder of the video, we perform online optimization by propagating the pose temporally. By capitalizing on the strong visual similarity between our generated textured mesh and the video observations, we drive this alignment using semantic feature loss and mask constraints, while simultaneously enforcing physical contact consistency. This approach proves significantly more stable than relying on noisy per-frame predictions or fragile SfM.

Comprehensive evaluations across benchmarks (HO3D, DexYCB) and diverse in-the-wild videos demonstrate the transformative impact of our approach. AGILE achieves state-of-the-art performance across all datasets, establishing a new standard for both accuracy and robustness. While prior methods suffer from high failure rates (up to 75%) on complex sequences, AGILE maintains a 100% success rate. Our analysis reveals a critical trade-off: while some prior methods optimize for local proximity—often allowing physical interpenetration—our approach prioritizes global geometric accuracy and non-penetration. Consequently, AGILE delivers digital twins that are validated via a real-to-sim retargeting pipeline, successfully driving dynamic interactions in a physics simulator.

Our contributions can be summarized as follows. First, we propose the first agentic HOI pipeline that integrates VLM-guided quality assessment with generative models, enabling the production of high-fidelity, watertight meshes independent of video occlusions. Second, we introduce a robust anchor-and-track optimization strategy that eliminates the dependency on brittle SfM by anchoring pose initialization at a single contact frame and propagating it via semantic and geometric alignment. Third, we incorporate physics-aware constraints to strictly enforce interaction stability and prevent penetration. Extensive experiments demonstrate that AGILE achieves state-of-the-art geometric accuracy and exceptional robustness across HO3D,

DexYCB, and challenging in-the-wild sequences.

2. Related Work

3D Hand Reconstruction. Monocular 3D hand reconstruction has evolved from fitting parametric models like MANO [22] to images [1, 17, 37, 38], towards recovering dynamic motion from video. While recent temporal approaches [35, 36] regress 4D trajectories, they often sacrifice the per-frame geometric precision essential for contact analysis. In our framework, we prioritize geometric fidelity to ensure accurate interaction modeling. Consequently, we leverage state-of-the-art estimators like WiLoR [18] to provide robust, high-fidelity initial hand meshes.

Generative 3D Object Reconstruction. The field is shifting from multi-view optimization (e.g., NeRF [15], Gaussian Splatting [10])—which requires dense, unoccluded coverage rarely found in interaction videos—to generative inference. Large Reconstruction Models (LRMs) [9, 25, 27, 33] and diffusion-based methods [12, 13] now generate assets from sparse inputs. However, single-view methods like SAM3D [26], while capable of end-to-end inference, inherently lack the capacity to aggregate multi-view cues from video. This limitation prevents them from resolving severe occlusions or maintaining texture consistency across views. We address this by proposing an agentic framework that intelligently fuses video evidence with generative priors, synthesizing watertight, textured assets that strictly align with video observations.

Hand-Object Interaction (HOI) Reconstruction. Reconstructing dynamic HOI is complicated by severe mutual occlusion. Early template-based [5, 6, 29, 34] or depth-dependent methods limit in-the-wild applicability. *Reconstruction-based methods* like HOLD [7] and BIGS [16] optimize implicit representations but yield fragmented, non-physical geometries under occlusion. Furthermore, their reliance on brittle Structure-from-Motion (SfM) initialization (e.g., COLMAP [23]) leads to frequent failures on textureless or moving objects. *Generative approaches* attempt to hallucinate missing regions; MagicHOI [31] integrates diffusion priors with NeRF but relies on Score Distillation Sampling (SDS), often producing over-smoothed meshes lacking simulation-ready detail. Crucially, it retains the fragility of SfM initialization. In contrast, AGILE eliminates the SfM bottleneck via a robust anchor-and-track strategy, delivering high-fidelity, simulation-ready digital twins.

3. Method

Given a monocular video of a hand-object interaction captured by a fixed camera, our goal is to reconstruct the 4D

trajectory of both the hand and the object, yielding high-fidelity, simulation-ready 3D assets, as illustrated in Figure 3. Unlike previous methods [7, 16] that rely on neural rendering and fragile Structure-from-Motion (SfM) initialization, we propose AGILE, a generative framework that shifts the paradigm from *reconstruction* to *agentic generation* for hand-object interaction reconstruction.

3.1. Agentic Textured Object Generation

A primary challenge in reconstructing hand-object interactions from monocular video is the severe occlusion of the object by the user’s hand. While neural rendering [10, 15] excels at view synthesis, it struggles to recover complete geometry from such partially visible data. Similarly, single-view generative methods like SAM3D [26] inherently suffer from information loss, yielding coarse geometries and low-fidelity textures that destabilize subsequent pose optimization. To overcome these limitations, it is essential to aggregate multi-view cues from the video using 2D generative priors to synthesize missing perspectives. However, the stochastic nature of diffusion models frequently introduces hallucinations that deviate from the actual object in the video. Reliably harnessing these priors therefore requires an intelligent mechanism capable of identifying the most informative reference frames and strictly filtering generated views for consistency—a capability missing in standard pipelines. To address this, we propose an agentic framework where a VLM supervisor acts as this intelligent critic, bridging the gap between noisy generative priors and rigorous video evidence.

VLM-Guided Multi-View Synthesis. As illustrated in Figure 2, our pipeline operates through a cascade of generative models steered by a VLM agent. Instead of relying on a single frame, the VLM first selects N informative keyframes (typically 1–4) from the input video to maximize viewpoint coverage. These frames prompt an image generation model to synthesize orthogonal views of the object. To ensure these hallucinations faithfully reflect the video content, we introduce a VLM-based critic. The VLM evaluates the consistency between generated views and original video frames, scoring them on geometry, texture, and material correspondence. Through a rejection sampling process, candidates falling below a strict consistency threshold are discarded and re-generated. This ensures that the input for 3D lifting is not only multi-view consistent but also faithful to the real-world observation. Implementation details are provided in the Supplementary Material.

3D Lifting and Mesh Refinement. The validated multi-view images are processed by a feed-forward 3D generation model [27] to produce an initial mesh. While geometrically plausible, raw outputs often suffer from irregular topology

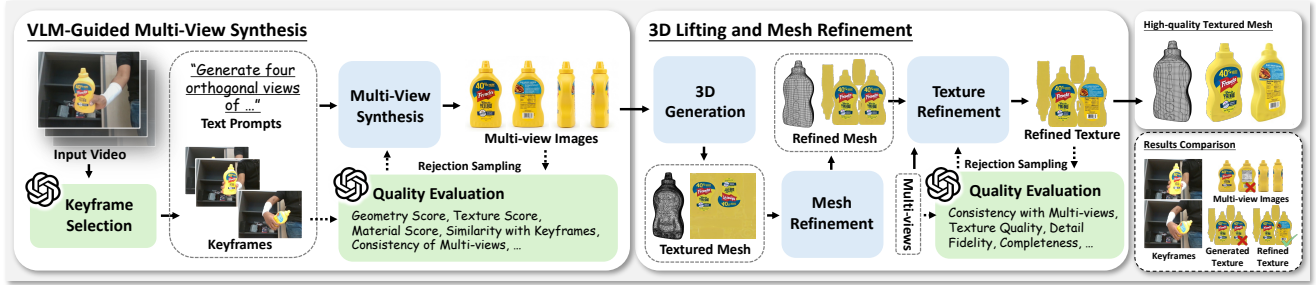


Figure 2. **Pipeline for Agentic Textured Object Generation.** A VLM agent first selects informative keyframes from the input video to guide multi-view synthesis. To ensure consistency, a VLM-based critic filters the generated views via rejection sampling. The validated images are then lifted to 3D, followed by automated topology optimization and texture refinement. As highlighted in the bottom-right comparison, this refinement step significantly enhances texture fidelity against the evaluated multi-views, yielding a high-quality, simulation-ready asset.

and blurry textures. To address this, we first apply automated retopology and UV unwrapping to create a clean, lightweight mesh optimized for physics simulation. Subsequently, we perform an *agentic texture refinement* step. The initial texture is enhanced using an image-to-image editing model conditioned on the evaluated high-resolution multi-view images to recover details. Crucially, as shown in Figure 2, this process is also supervised by the VLM agent. The VLM critic evaluates the refined texture against the multi-views via rejection sampling, ensuring strict visual fidelity and discarding any hallucinated artifacts. This rigorous quality control is motivated by two downstream requirements: (1) Foundation models used for pose initialization (e.g., FoundationPose [32]) rely heavily on sharp textual features for robust matching; and (2) our subsequent optimization utilizes DINO features, which demand high visual fidelity to maintain accuracy. This refinement yields a simulation-ready asset with photo-realistic appearance and explicit topology.

Our agentic framework offers distinct advantages over traditional baselines. First, it enables fully automated asset acquisition from arbitrary videos, effectively bypassing the failure modes of photogrammetry under heavy occlusion. Second, by continually aggregating temporal cues via VLM supervision, we ensure exceptional visual consistency between the generated asset and the video. Finally, unlike implicit representations, our approach directly produces clean, watertight meshes with high-frequency textures, providing a robust initialization that is critical for the stability of subsequent interaction tracking and physics simulation.

3.2. Initialization of Pose and Scale

To enable robust tracking without relying on brittle Structure-from-Motion pipelines, we establish a consistent metric initialization for both the hand and object. First, we extract essential scene information, including segmentation

masks, camera intrinsics, and estimated metric depth. Second, we recover the metric geometry of the hand, comprising its 6D pose, global scale, and 2D joint projections. Finally, we estimate the object’s global scale across the sequence and initialize its pose at the interaction onset frame.

Data Preprocessing. For each input video frame, we extract a set of key components. Specifically, we employ the monocular metric depth estimator MoGe-2 [30] to obtain the camera intrinsic matrix \mathbf{K} and a per-frame metric depth map $\mathbf{D} \in \mathbb{R}^{H \times W}$. Simultaneously, we use SAM2 [21] to acquire precise segmentation masks for both the hand (\mathbf{M}_h) and the object (\mathbf{M}_o). Given our static camera assumption, the camera coordinate system serves as the world frame, with extrinsic parameters fixed as the identity matrix. These preprocessed priors form the foundational inputs for all subsequent stages.

Metric Hand Initialization. We utilize the preprocessed data to initialize a physically plausible hand model. We first employ the off-the-shelf estimator WiLoR [18] to predict the MANO [22] parameters for each frame, including shape β , pose θ , global rotation $\mathbf{R}_h \in SO(3)$, and the corresponding 2D keypoint annotations $\mathbf{J}_{2D} \in \mathbb{R}^{21 \times 2}$. Since WiLoR provides reliable rotation estimates, we fix \mathbf{R}_h and focus on recovering the missing metric scale and translation. To determine the global scale $s_h \in \mathbb{R}^+$, we unproject the masked hand pixels into 3D point clouds using the metric depth map \mathbf{D} . We align the MANO mesh to these depth observations using a constrained Iterative Closest Point (ICP) algorithm [3]. In this step, we hold \mathbf{R}_h fixed and optimize for s_h and a temporary translation to minimize the model-to-scan distance. Finally, to ensure accurate image alignment, we fix s_h , \mathbf{R}_h , and the intrinsics \mathbf{K} , and solve for the per-frame translation $\mathbf{T}_h \in \mathbb{R}^3$ via a Perspective-n-Point (PnP) approach, utilizing the 3D model

joints and the predicted 2D keypoints \mathbf{J}_{2D} .

Object Pose and Scale Estimation. Once the canonical object mesh is created (Sec. 3.1), we align it to the video observations using a scale-first strategy. We first estimate the object’s global metric scale s_o by applying the same constrained ICP algorithm used for the hand, aligning the generated mesh with the unprojected object point clouds across all available frames. Next, we identify the *interaction onset frame* (IOF), defined as the moment the object mask \mathbf{M}_o exhibits significant displacement. Finally, to determine the initial object pose $[\mathbf{R}_o^{IOF}, \mathbf{T}_o^{IOF}]$, we apply Foundation-Pose [32] at the IOF. This estimator takes the RGB frame, the metric depth map, and the generated mesh pre-scaled by s_o as input, ensuring the estimated pose is metrically consistent with the scene.

3.3. Hand-Object Interaction Optimization

To ensure pixel-level alignment and physical consistency, we employ a bi-directional online optimization strategy anchored at the *interaction onset frame* (IOF) (identified in Sec. 3.2). Starting from the IOF, we propagate the optimization frame-by-frame towards both the start and end of the video sequence. At the IOF, we jointly optimize the hand and object poses along with the object’s anisotropic scale s_o to establish a reliable canonical geometry. For all subsequent frames, s_o is frozen, and we perform the following two-step optimization per frame:

Step 1: Hand Translation Refinement. For the current frame, we first refine the hand trajectory. Relying on the robust orientation estimates from the initialization stage, we fix the hand rotation \mathbf{R}_h and scale s_h . We exclusively optimize the translation \mathbf{T}_h to align the mesh with 2D observations. This step is driven solely by the *joint reprojection loss* ($\mathcal{L}_{\text{joint}}$), which minimizes the Euclidean distance between projected 3D joints and 2D detections. This strictly geometric update ensures the hand serves as a stable anchor for the object.

Step 2: Interaction-Aware Object Tracking. With the refined hand pose fixed, we optimize the object’s rigid pose $(\mathbf{R}_o, \mathbf{T}_o)$. To handle rapid motion or occlusion, the object pose is initialized using the result from the preceding processed frame. During this stage, we minimize a composite objective function to ensure visual and physical fidelity:

$$\mathcal{L}_{\text{obj}} = \lambda_{\text{mask}} \mathcal{L}_{\text{mask}} + \lambda_{\text{dino}} \mathcal{L}_{\text{dino}} + \lambda_{\text{interact}} \mathcal{L}_{\text{interact}}. \quad (1)$$

Here, $\mathcal{L}_{\text{mask}}$ enforces silhouette alignment, and $\mathcal{L}_{\text{dino}}$ maintains semantic feature consistency using DINOv3 [24] to mitigate texture ambiguity. Crucially, $\mathcal{L}_{\text{interact}}$ penalizes interpenetration and encourages surface attraction, ensuring the object remains tightly locked to the hand in a physically plausible manner.

Joint Reprojection Loss ($\mathcal{L}_{\text{joint}}$). To spatially anchor the hand pose using reliable 2D cues, we introduce a joint reprojection loss. Let $\Pi(\cdot)$ denote the perspective projection function given the camera intrinsics. We constrain the projected positions of the 3D hand joints \mathbf{J}_{3D} to match the pre-processed 2D keypoint annotations $\mathbf{J}_{2D} \in \mathbb{R}^{21 \times 2}$. The loss is defined as the mean squared error (MSE):

$$\mathcal{L}_{\text{joint}} = \frac{1}{N_j} \sum_{i=1}^{N_j} \|\Pi(\mathbf{J}_{3D}^{(i)}) - \mathbf{J}_{2D}^{(i)}\|_2^2. \quad (2)$$

This term ensures the estimated hand geometry remains consistent with the detected anatomical landmarks on the image plane.

Mask Alignment Loss ($\mathcal{L}_{\text{mask}}$). To ensure the reconstructed geometry aligns with the visual evidence, we employ a mask alignment loss. This term measures the discrepancy between the rendered alpha silhouette \mathbf{A}_{ren} and the ground-truth segmentation mask \mathbf{M}_{gt} . We formulate this as the L_2 distance between the two maps:

$$\mathcal{L}_{\text{mask}} = \|\mathbf{A}_{\text{ren}} - \mathbf{M}_{\text{gt}}\|_2^2. \quad (3)$$

By minimizing this difference, the optimization drives the rendered mesh to tightly fit the observed pixel-level silhouette, effectively handling occlusion boundaries.

Semantic Feature Loss ($\mathcal{L}_{\text{dino}}$). To mitigate tracking ambiguities caused by partial occlusions or textureless regions, we leverage deep semantic features from a pre-trained Vision Transformer, specifically DINOv3 [24]. Unlike pixel-wise photometric losses, semantic features provide robust correspondences invariant to local lighting changes.

We establish explicit 3D-to-2D semantic correspondences through a sampling-based approach. Periodically, we sample a set of N_p visible points $\mathcal{P}_{\text{can}} = \{\mathbf{p}_i\}_{i=1}^{N_p}$ on the canonical object surface. For each point \mathbf{p}_i , we compute a *feature similarity map* $\mathbf{S}_i \in \mathbb{R}^{H_f \times W_f}$ by correlating its feature vector (extracted from the rendered view) against the dense feature map of the target ground-truth image \mathbf{F}_{gt} . This similarity map \mathbf{S}_i encodes the likelihood of the point \mathbf{p}_i corresponding to each spatial location in the target image.

During optimization, we transform these canonical points into the current camera frame using the estimated object pose $(\mathbf{R}_o, \mathbf{T}_o)$ and scale s_o , and project them to obtain 2D coordinates $\mathbf{u}_i = \Pi(\mathbf{R}_o(\mathbf{s}_o \odot \mathbf{p}_i) + \mathbf{T}_o)$. The loss is formulated to maximize the semantic similarity at the projected locations, weighted by an occlusion mask to ignore unreliable regions:

$$\mathcal{L}_{\text{dino}} = -\frac{1}{|\mathcal{V}|} \sum_{i \in \mathcal{V}} \mathcal{M}_{\text{occ}}(\mathbf{u}_i) \cdot \text{sample}(\mathbf{S}_i, \mathbf{u}_i), \quad (4)$$

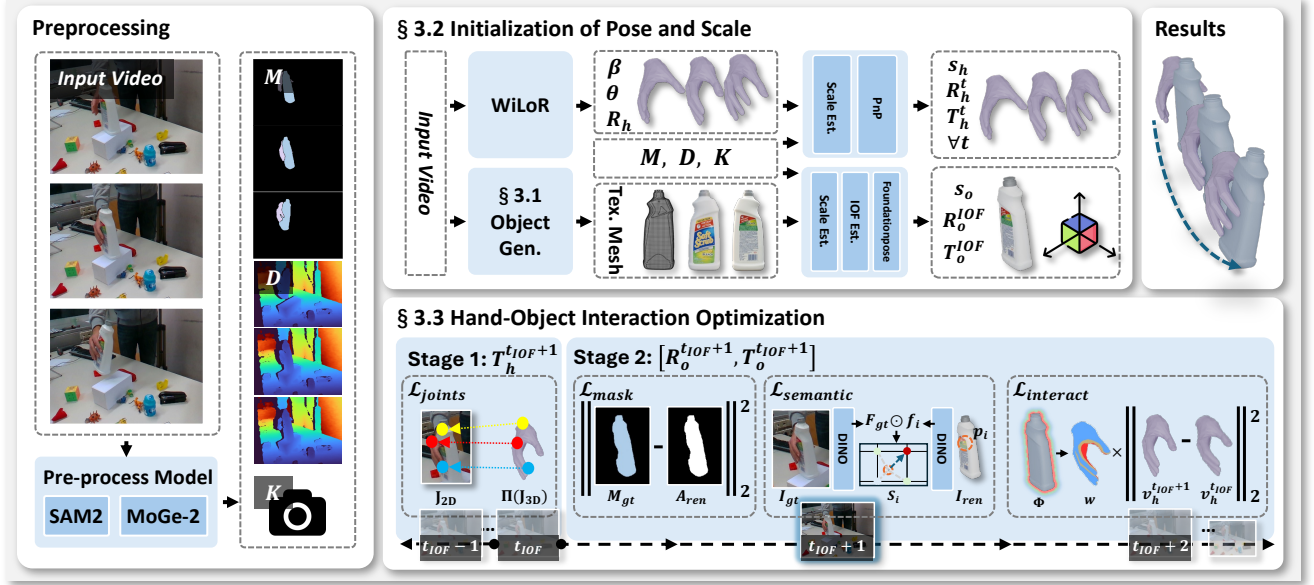


Figure 3. **Pipeline of AGILE.** Our framework processes the input video in three phases: (1) **Agentic Generation** (§3.1): A VLM-guided loop extracts keyframes and supervises the synthesis of a watertight, textured object mesh \mathcal{M}_o , utilizing rejection sampling to ensure visual fidelity. (2) **SfM-Free Initialization** (§3.2): We decouple metric scale and pose. The hand is initialized via WiLoR, while the object pose is anchored at the Interaction Onset Frame (IOF) using a foundation model. (3) **Contact-Aware Optimization** (§3.3): A bi-directional tracking process refines the trajectories. We stabilize the hand via geometric alignment and track the object using semantic (\mathcal{L}_{dino}) and interaction constraints ($\mathcal{L}_{interact}$) to ensure physical plausibility.

where \mathcal{V} denotes the set of currently visible sampled points, \mathcal{M}_{occ} is the binary occlusion mask (0 for occluded regions), and $\text{sample}(\cdot)$ represents bilinear interpolation of the similarity map at coordinates \mathbf{u}_i . By maximizing this similarity, the optimization drives the object pose to align its semantic parts with the corresponding regions in the video frame.

Interaction Stability Loss ($\mathcal{L}_{interact}$). Given the severe occlusion of the object during manipulation, strictly geometric cues from the image are often insufficient. To resolve this, we impose a physical prior that the relative spatial configuration between the hand and the object remains stable during a grasp. This enforces the assumption that the hand and object move approximately as a rigid aggregate during interaction.

Specifically, we formulate a interaction stability loss in the object’s canonical coordinate system. Let $\mathbf{V}_h^{(t)} \in \mathbb{R}^{N \times 3}$ denote the hand vertices in the camera frame at time t , and let $(\mathbf{R}_o^{(t)}, \mathbf{T}_o^{(t)})$ be the estimated object pose. We map the current hand vertices into the current object’s local frame via the inverse transformation:

$$\tilde{\mathbf{v}}_{h,i}^{(t)} = (\mathbf{R}_o^{(t)})^\top (\mathbf{v}_{h,i}^{(t)} - \mathbf{T}_o^{(t)}), \quad (5)$$

where $\mathbf{v}_{h,i}^{(t)}$ is the i -th vertex of the hand. We then minimize the displacement of these local coordinates relative to their positions in the previous tracked frame ($t - 1$).

Crucially, to ensure the constraint applies only to the effective grasping regions, we compute a vertex-wise weight map $\mathbf{w} \in \mathbb{R}^N$ based on the object’s Signed Distance Function (SDF), denoted as $\Phi(\cdot)$. We calculate the distance of the previous hand vertices to the object surface: $d_i = \max(0, \Phi(\tilde{\mathbf{v}}_{h,i}^{(t-1)}))$. The weights are then derived using a soft gating function:

$$w_i = 1 - \tanh(\sigma \cdot d_i), \quad (6)$$

where σ is a scaling factor controlling the sensitivity of the fall-off. This formulation assigns high weights ($w_i \approx 1$) to vertices in close proximity to the object surface while suppressing the influence of non-interacting fingers. The final loss is defined as:

$$\mathcal{L}_{interact} = \frac{1}{N} \sum_{i=1}^N w_i \cdot \|\tilde{\mathbf{v}}_{h,i}^{(t)} - \tilde{\mathbf{v}}_{h,i}^{(t-1)}\|_2. \quad (7)$$

Minimizing this term effectively “locks” the object to the grasping hand parts, preventing unnatural sliding or jitter when visual features are ambiguous.

In summary, this optimization framework prioritizes reconstruction fidelity and physical consistency. By directly optimizing explicit 3D meshes, our method allows for the seamless integration of 2D visual supervision with 3D inter-

action constraints, which is often difficult for implicit representations. This design effectively resolves tracking ambiguities caused by severe hand occlusions. Furthermore, our decoupled, interaction-aware strategy ensures that the reconstructed motion is not only pixel-aligned but also physically grounded, preserving the high-quality geometry and texture assets generated in the previous stage.

4. Experiments

Datasets. We evaluate AGILE on both standard benchmarks and challenging in-the-wild sequences. For quantitative evaluation, we utilize the **DexYCB** dataset [2], selecting 20 diverse trajectories that cover a wide range of object categories and interaction types. To assess robustness under severe occlusion, we employ the **HO3D-v3** dataset [8], testing on 18 sequences following the protocol of HOLD [7]. Furthermore, to demonstrate generalization capabilities, we curate an **In-the-Wild** dataset. This collection integrates sequences from prior work [7] with self-captured footage, specifically targeting objects with complex geometries and intricate manipulation patterns to verify robustness in arbitrary settings.

Baselines. We benchmark our framework against state-of-the-art approaches in monocular hand-object reconstruction. Specifically, we compare with **HOLD** [7], which reconstructs interactions via implicit neural rendering, and **MagicHOI** [31], a recent method leveraging diffusion-based priors for geometry generation. Detailed hyperparameters, implementation details, and runtime analysis are provided in the Supp.

Metrics. We evaluate system performance focusing on geometric fidelity, interaction plausibility, and robustness. (1) *Hand Accuracy*: We report the Root-relative Mean Per-Joint Position Error (MPJPE) in millimeters. (2) *Object Geometry*: Following the protocol of HOLD [7], we evaluate reconstruction quality using Chamfer Distance (CD) in squared centimeters (cm^2) and F-scores at 5mm and 10mm thresholds (F@5mm, F@10mm). (3) *Interaction Quality*: We compute the Hand-relative Chamfer Distance (CD_h), also in cm^2 , by aligning the object to the hand’s root frame to measure relative spatial consistency. (4) *Robustness*: Crucially, we report the *Success Rate* (SR). A sequence is considered a failure if the method encounters initialization breakdown (e.g., SfM collapse) or suffers from catastrophic tracking drift.

4.1. Comparisons

We conduct extensive quantitative and qualitative comparisons against state-of-the-art methods on DexYCB and HO3D-v3 datasets.

Quantitative Evaluation. As presented in Table 1, AGILE establishes a new state-of-the-art benchmark for monocular HOI reconstruction. We consistently outperform both optimization-based (HOLD) and generative-based (MagicHOI) baselines across all metrics. In terms of geometric fidelity, AGILE achieves a Chamfer Distance (CD) of **0.52 cm²** on DexYCB, reducing the reconstruction error by nearly **75%** compared to MagicHOI (2.05 cm²). This substantial gap highlights the advantage of our agentic generation pipeline over standard SfM-based initialization, which often yields noisy or incomplete geometry.

Interaction Stability and Drift. A critical differentiator lies in the interaction quality (CD_h). Prior methods suffer from severe *interaction drift* due to scale ambiguity and lack of physical constraints. MagicHOI, for instance, exhibits a drastically high CD_h of 661.90 cm², indicating that the object frequently loses contact or drifts far from the hand. In contrast, AGILE maintains a significantly lower CD_h of 94.60 cm². This confirms that our *Contact-Aware Optimization* effectively anchors the object to the hand, ensuring the reconstruction remains physically cohesive and valid for simulation.

Robustness and Survivor Bias. The superiority of AGILE is most evident when analyzing system robustness. As shown in the Success Rate (SR) column, baselines exhibit high failure rates on DexYCB: MagicHOI fails on 75% of the sequences, and HOLD fails on 55%. It is important to note that the metrics reported for these baselines are biased, as they are averaged only over the *easiest* subset of sequences where initialization succeeded (Survivor Bias). Conversely, AGILE achieves a 100% Success Rate, evaluating on the entire dataset including the most challenging occlusion cases. Remarkably, even while averaging over these harder samples, AGILE still achieves a lower global pose error (MPJPE: 19.06 mm) than MagicHOI (21.20 mm) computed on its easy subset. This demonstrates that AGILE is not only more robust but also fundamentally more accurate.

Qualitative Evaluation. Qualitative comparisons in Figure 4 corroborate the quantitative findings. Baselines often produce fragmented geometry or suffer from "floating object" artifacts where the object drifts away from the interaction zone. Leveraging generative priors, AGILE reconstructs watertight, high-fidelity meshes. Moreover, the temporal consistency of our results eliminates the jitter observed in prior arts, faithfully reflecting the physical reality of the input video.

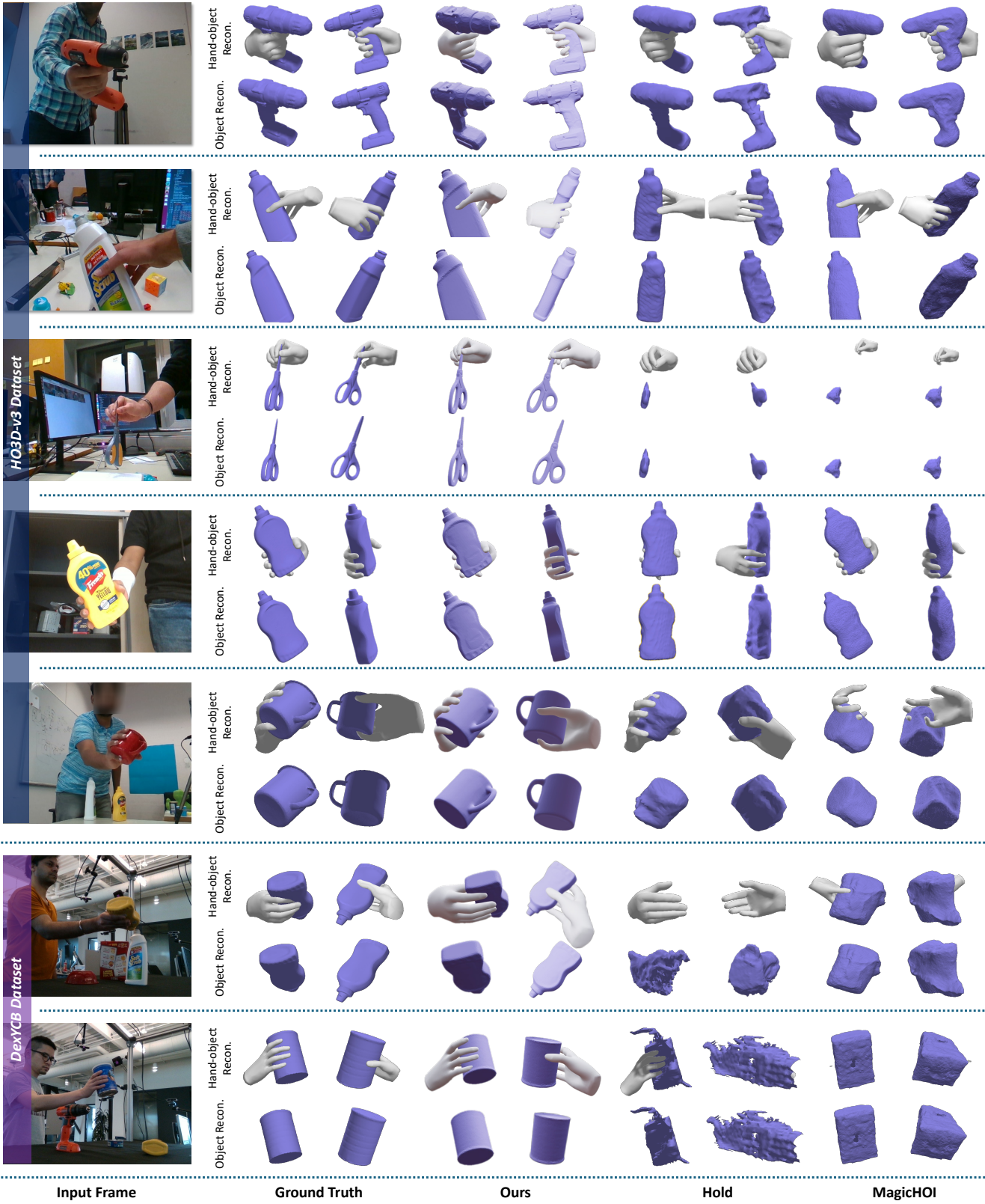


Figure 4. **Qualitative Comparison.** We compare our reconstructed hands and objects with baseline methods on the HO3D-v3 and DexYCB dataset, showing camera views as well as side views of the object-only and hand-object interaction results.



Figure 5. **Qualitative Results of Agentic Generation.** We visualize the intermediate stages of our pipeline across diverse object categories. Despite severe hand occlusion in the input keyframes, our VLM-guided approach successfully synthesizes consistent multi-view images and reconstructs high-fidelity 3D meshes. Notably, the *texture refinement* step significantly enhances surface details and sharpness compared to the initial raw generation.

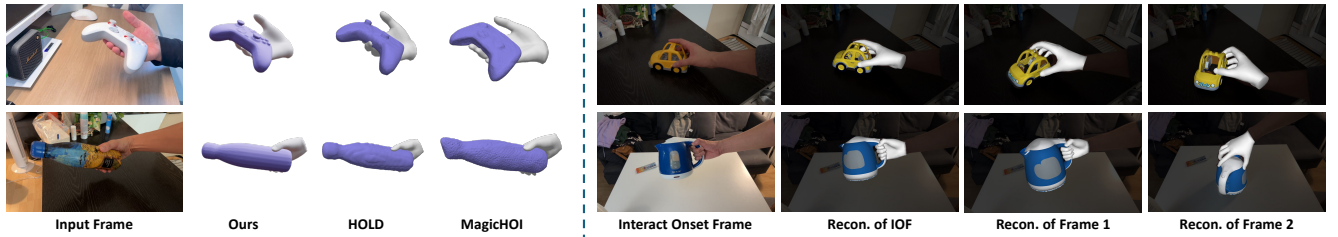


Figure 6. **Qualitative Evaluation on In-the-Wild Sequences.** (Left) Comparison against state-of-the-art baselines. While HOLD [7] and MagicHOI [31] suffer from geometric noise or over-smoothed artifacts due to unreliable initialization, AGILE recovers clean, high-fidelity meshes. (Right) Our reconstruction results across temporal sequences. Starting from the Interaction Onset Frame (IOF), our anchor-and-track strategy maintains robust alignment and physical plausibility throughout the dynamic interaction.

4.2. Ablation Study

We conduct a detailed ablation study on the HO3D dataset to dissect the contribution of each component in our framework. We evaluate the impact on three key dimensions: Hand Pose Accuracy (MPJPE), Object Geometric Fidelity (CD), and Interaction Alignment (CD_h). The quantitative results are summarized in Table 2.

(a) Full Model. Our complete pipeline achieves the best performance across all metrics, validating the synergy between high-fidelity asset generation and physics-aware tracking.

Impact of Agentic Generation Modules. We first analyze the components responsible for creating the 3D asset, which serves as the foundation for subsequent tracking.

(b) w/o Agentic Multi-view Generation. In this variant, we disable the VLM-guided multi-view generation and directly lift the 3D mesh from a single input image. This leads to a catastrophic deterioration in object geometry, with CD rising from 0.27 to 2.85. Without the multi-view consistency enforced by our agentic loop, the model hallucinates incor-

rect geometry for occluded regions, creating a mesh that fails to align with video observations from varying viewpoints.

(c) w/o Texture Refine. Here, we skip the texture baking and refinement step. This ablation proves critical: high-quality texture is not merely for visual aesthetics but is a prerequisite for robust tracking. Since both our initialization (via FoundationPose) and our semantic consistency loss rely on discriminative surface features, noisy or blurred textures lead to initialization drift, causing a noticeable rise in interaction error (CD_h).

Impact of Optimization Objectives. Next, we evaluate the loss functions used during the decoupled optimization stages.

(d) w/o \mathcal{L}_{joint} . In this variant, the hand pose relies solely on the initial PnP estimation without further optimization. The significant degradation in MPJPE confirms that PnP initialization alone is insufficient for high-precision tracking. \mathcal{L}_{joint} is indispensable for refining these initial estimates to resolve depth ambiguities and ensure temporally consistent hand articulation.

Table 1. **Quantitative comparison on DexYCB and HO3D-v3 datasets.** The **best** results are highlighted in bold, and the second best are underlined. Baseline metrics (\dagger) are averaged over the *successful subset* only, creating a survivor bias.

Method	DexYCB Dataset						HO3D-v3 Dataset					
	MPJPE (mm) \downarrow	CD (cm^2) \downarrow	F@5 (%) \uparrow	F@10 (%) \uparrow	CD _h (cm^2) \downarrow	SR (%) \uparrow	MPJPE (mm) \downarrow	CD (cm^2) \downarrow	F@5 (%) \uparrow	F@10 (%) \uparrow	CD _h (cm^2) \downarrow	SR (%) \uparrow
HOLD \dagger [7]	30.86	19.30	33.20	54.94	<u>170.9</u>	45.0	22.09	1.11	<u>81.75</u>	<u>92.42</u>	<u>18.66</u>	100.0
MagicHOI \dagger [31]	21.20	<u>2.05</u>	<u>45.67</u>	<u>67.14</u>	661.90	25.0	<u>7.38</u>	<u>0.90</u>	76.74	91.59	21.81	83.3
Ours	19.06	0.52	83.21	95.43	94.60	100.0	3.92	0.27	86.63	97.77	15.81	100.0



Figure 7. **Qualitative Ablation Study.** Visual comparisons demonstrate that removing key components—such as agentic generation or interaction constraints—leads to severe geometric artifacts, texture degradation, and physical violations (e.g., interpenetration), validating the necessity of our full pipeline.

Table 2. Detailed ablation study on the HO3D dataset. We systematically evaluate the impact of generative components and optimization objectives.

Model Variant	Hand		Object Geometry		Interaction
	MPJPE \downarrow	CD \downarrow	CD \downarrow	F@5mm \uparrow	CD _h \downarrow
(a) AGILE (Full)	3.92	0.27	86.63	15.81	
<i>Generative Components</i>					
(b) w/o Agentic Multi-view Gen.	4.02	2.85	30.12	40.12	
(c) w/o Texture Refine.	4.16	0.30	86.02	20.18	
<i>Optimization Objectives</i>					
(d) w/o \mathcal{L}_{joint}	5.06	0.33	84.93	19.37	
(e) w/o \mathcal{L}_{mask}	3.97	0.40	81.14	23.99	
(f) w/o \mathcal{L}_{dino}	4.13	0.34	84.36	21.64	
(g) w/o $\mathcal{L}_{interact}$	4.17	0.35	86.10	54.40	

(e) *w/o \mathcal{L}_{mask}* . This component provides the strongest pixel-level geometric constraint for the rigid object. Although the object scale is pre-initialized, \mathcal{L}_{mask} is critical for fine-tuning the scale at the anchor frame and guiding precise 6D pose optimization throughout the sequence. Without this constraint, the object pose fails to strictly adhere to visual boundaries, resulting in misalignment that negatively impacts both CD and F-scores.

(f) *w/o \mathcal{L}_{dino}* . We ablate the DINO-based semantic feature loss. In the absence of this consistency term, object tracking becomes prone to drift, particularly in textureless regions or under motion blur. The increase in CD_h confirms that semantic descriptors provide robust correspondence where pixel-level metrics alone are insufficient.

(g) *w/o $\mathcal{L}_{interact}$* . Finally, removing the interaction stability loss leads to severe physical violations. Without this constraint, the object tends to slide unnaturally or penetrate the

hand mesh to minimize surface distance. Consequently, the fine-grained interaction quality degrades drastically (CD_h spikes to 54.40), highlighting the necessity of SDF-based priors for physically plausible reconstruction.

4.3. Application: Real-to-Sim Retargeting

To validate the physical plausibility of our reconstructions for Embodied AI, we implement a scalable Real-to-Sim pipeline. We import the reconstructed sequence into Isaac Gym [14] and map the human hand motion to a multi-fingered robotic hand (e.g., Shadow) using kinematic optimization [19], with the agentic-generated mesh serving as a dynamic rigid body.

As illustrated in Figure 8, AGILE effectively bridges the gap between video and simulation: (1) *Simulation-Ready Assets*: Our generated meshes are watertight and topologically clean, enabling stable collision detection without manual post-processing. (2) *Robust Kinematic Transfer*: Crucially, stable grasps are maintained solely through kinematic mapping, without auxiliary reinforcement learning or physics-based correction. This stability serves as a rigorous validation of our reconstruction quality, confirming that AGILE recovers accurate relative poses and contact states. By automating this process, our framework unlocks the potential to curate large-scale manipulation datasets from unconstrained monocular videos for generalist policy learning.



Figure 8. **Real-to-Sim retargeting results**, demonstrating that AGILE enables stable kinematic transfer of reconstructed human hand-object interactions to a multi-fingered robotic hand without physics-based correction.

5. Conclusion

In this work, we presented AGILE, a robust framework addressing the persistent challenges of incomplete geometry and brittle initialization in large-scale HOI reconstruction. By shifting the paradigm from *reconstruction-based* optimization to *agentic generation*, we leverage VLM-guided priors to synthesize high-fidelity, watertight object meshes even under severe occlusion. Furthermore, our *anchor-and-track* strategy eliminates the dependency on fragile SfM pipelines, enabling stable pose estimation on challenging in-the-wild videos where prior methods fail. Extensive experiments confirm that AGILE achieves state-of-the-art accuracy and exceptional robustness, producing simulation-ready digital twins that effectively bridge the gap between visual observation and physical simulation.

Limitations and Future Work. Despite these advancements, our framework inherently inherits limitations from the off-the-shelf foundation models used for depth estimation and initialization. Consequently, extreme scenarios that challenge these priors—such as transparent objects, highly reflective surfaces, or erratic camera motions—may lead to scale drift or tracking errors that our optimization cannot fully recover. Additionally, our current generative pipeline assumes rigid objects; extending this agentic approach to articulated or deformable objects remains a promising direction for future research. Nevertheless, we believe this work marks a significant step towards the scalable acquisition of embodied skills from the vast repository of internet video data.

References

[1] Adnane Boukhayma, Rodrigo de Bem, and Philip HS Torr. 3d hand shape and pose from images in the wild. In *Proceedings of the IEEE/CVF conference on computer vision and pattern recognition*, pages 10843–10852, 2019. 3

[2] Yu-Wei Chao, Wei Yang, Yu Xiang, Pavlo Molchanov, Ankur Handa, Jonathan Tremblay, Yashraj S Narang, Karl Van Wyk, Umar Iqbal, Stan Birchfield, et al. Dexycb: A benchmark for capturing hand grasping of objects. In *Proceedings of the IEEE/CVF conference on computer vision and pattern recognition*, pages 9044–9053, 2021. 2, 7, 1

[3] Dmitry Chetverikov, Dmitry Svirko, Dmitry Stepanov, and Pavel Krsek. The trimmed iterative closest point algorithm. In *2002 International Conference on Pattern Recognition*, pages 545–548. IEEE, 2002. 4

[4] Gheorghe Comanici, Eric Bieber, Mike Schaeckermann, Ice Pasupat, Noveen Sachdeva, Inderjit Dhillon, Marcel Blissestein, Ori Ram, Dan Zhang, Evan Rosen, et al. Gemini 2.5: Pushing the frontier with advanced reasoning, multimodality, long context, and next generation agentic capabilities. *arXiv preprint arXiv:2507.06261*, 2025. 1

[5] Enric Corona, Albert Pumarola, Guillem Alenya, Francesc Moreno-Noguer, and Gr  gory Rogez. Ganhand: Predicting human grasp affordances in multi-object scenes. In *Proceedings of the IEEE/CVF conference on computer vision and pattern recognition*, pages 5031–5041, 2020. 3

[6] Zicong Fan, Takehiko Ohkawa, Linlin Yang, Nie Lin, Zhihan Zhou, Shihao Zhou, Jiajun Liang, Zhong Gao, Xuanyang Zhang, Xue Zhang, et al. Benchmarks and challenges in pose estimation for egocentric hand interactions with objects. In *European Conference on Computer Vision*, pages 428–448. Springer, 2024. 3

[7] Zicong Fan, Maria Parelli, Maria Eleni Kadoglou, Xu Chen, Muhammed Kocabas, Michael J Black, and Otmar Hilliges. Hold: Category-agnostic 3d reconstruction of interacting hands and objects from video. In *Proceedings of the IEEE/CVF Conference on Computer Vision and Pattern Recognition*, pages 494–504, 2024. 2, 3, 7, 9, 10

[8] Shreyas Hampali, Mahdi Rad, Markus Oberweger, and Vincent Lepetit. Honnote: A method for 3d annotation of hand and object poses. In *Proceedings of the IEEE/CVF conference on computer vision and pattern recognition*, pages 3196–3206, 2020. 7, 1

[9] Yicong Hong, Kai Zhang, Jiuxiang Gu, Sai Bi, Yang Zhou, Difan Liu, Feng Liu, Kalyan Sunkavalli, Trung Bui, and Hao Tan. Lrm: Large reconstruction model for single image to 3d. *arXiv preprint arXiv:2311.04400*, 2023. 3

[10] Bernhard Kerbl, Georgios Kopanas, Thomas Leimkühler, and George Drettakis. 3d gaussian splatting for real-time radiance field rendering. *ACM Trans. Graph.*, 42(4):139–1, 2023. 2, 3

[11] Diederik P Kingma. Adam: A method for stochastic optimization. *arXiv preprint arXiv:1412.6980*, 2014. 1

[12] Ruoshi Liu, Rundi Wu, Basile Van Hoorick, Pavel Tokmakov, Sergey Zakharov, and Carl Vondrick. Zero-1-to-3: Zero-shot one image to 3d object. In *Proceedings of the IEEE/CVF international conference on computer vision*, pages 9298–9309, 2023. 3

[13] Xiaoxiao Long, Yuan-Chen Guo, Cheng Lin, Yuan Liu, Zhiyang Dou, Lingjie Liu, Yuexin Ma, Song-Hai Zhang, Marc Habermann, Christian Theobalt, et al. Wonder3d: Single image to 3d using cross-domain diffusion. In *Proceedings of the IEEE/CVF conference on computer vision and pattern recognition*, pages 9970–9980, 2024. 3

[14] Viktor Makoviychuk, Lukasz Wawrzyniak, Yunrong Guo, Michelle Lu, Kier Storey, Miles Macklin, David Hoeller, Nikita Rudin, Arthur Allshire, Ankur Handa, and Gavriel State. Isaac gym: High performance gpu-based physics simulation for robot learning, 2021. 10

[15] Ben Mildenhall, Pratul P Srinivasan, Matthew Tancik, Jonathan T Barron, Ravi Ramamoorthi, and Ren Ng. Nerf: Representing scenes as neural radiance fields for view synthesis. *Communications of the ACM*, 65(1):99–106, 2021. 2, 3

[16] Jeongwan On, Kyeonghwan Gwak, Gunyoung Kang, Junuk Cha, Soohyun Hwang, Hyein Hwang, and Seungryul Baek. Bigs: Bimanual category-agnostic interaction reconstruction from monocular videos via 3d gaussian splatting. In *Proceedings of the Computer Vision and Pattern Recognition Conference*, pages 17437–17447, 2025. 2, 3

[17] Georgios Pavlakos, Dandan Shan, Ilija Radosavovic, Angjoo Kanazawa, David Fouhey, and Jitendra Malik. Reconstructing hands in 3d with transformers. In *Proceedings of the IEEE/CVF Conference on Computer Vision and Pattern Recognition*, pages 9826–9836, 2024. 3

[18] Rolandos Alexandros Potamias, Jinglei Zhang, Jiankang Deng, and Stefanos Zafeiriou. Wilor: End-to-end 3d hand localization and reconstruction in-the-wild. In *Proceedings of the Computer Vision and Pattern Recognition Conference*, pages 12242–12254, 2025. 3, 4

[19] Yuzhe Qin, Wei Yang, Binghao Huang, Karl Van Wyk, Hao Su, Xiaolong Wang, Yu-Wei Chao, and Dieter Fox. Anyteleop: A general vision-based dexterous robot arm-hand teleoperation system. In *Robotics: Science and Systems*, 2023. 10

[20] Nikhila Ravi, Jeremy Reizenstein, David Novotny, Taylor Gordon, Wan-Yen Lo, Justin Johnson, and Georgia Gkioxari. Accelerating 3d deep learning with pytorch3d. *arXiv preprint arXiv:2007.08501*, 2020. 1

[21] Nikhila Ravi, Valentin Gabeur, Yuan-Ting Hu, Ronghang Hu, Chaitanya Ryali, Tengyu Ma, Haitham Khedr, Roman Rädle, Chloe Rolland, Laura Gustafson, et al. Sam 2: Segment anything in images and videos. *arXiv preprint arXiv:2408.00714*, 2024. 4, 1

[22] Javier Romero, Dimitrios Tzionas, and Michael J Black. Embodied hands: Modeling and capturing hands and bodies together. *arXiv preprint arXiv:2201.02610*, 2022. 3, 4

[23] Johannes Lutz Schönberger and Jan-Michael Frahm. Structure-from-motion revisited. In *Conference on Computer Vision and Pattern Recognition (CVPR)*, 2016. 2, 3

[24] Oriane Siméoni, Huy V. Vo, Maximilian Seitzer, Federico Baldassarre, Maxime Oquab, Cijo Jose, Vasil Khalidov, Marc Szafraniec, Seungeun Yi, Michaël Ramamonjisoa, Francisco Massa, Daniel Haziza, Luca Wehrstedt, Jianyuan Wang, Timothée Darcel, Théo Moutakanni, Leonel Sentana, Claire Roberts, Andrea Vedaldi, Jamie Tolan, John Brandt, Camille Couprie, Julien Mairal, Hervé Jégou, Patrick Labatut, and Piotr Bojanowski. DINov3, 2025. 5

[25] Jiaxiang Tang, Zhaoxi Chen, Xiaokang Chen, Tengfei Wang, Gang Zeng, and Ziwei Liu. Lgm: Large multi-view gaussian model for high-resolution 3d content creation. In *European Conference on Computer Vision*, pages 1–18. Springer, 2024. 3

[26] SAM 3D Team, Xingyu Chen, Fu-Jen Chu, Pierre Gleize, Kevin J Liang, Alexander Sax, Hao Tang, Weiyao Wang, Michelle Guo, Thibaut Hardin, Xiang Li, Aohan Lin, Jiawei Liu, Ziqi Ma, Anushka Sagar, Bowen Song, Xiaodong Wang, Jianing Yang, Bowen Zhang, Piotr Dollár, Georgia Gkioxari, Matt Feiszli, and Jitendra Malik. Sam 3d: 3dfy anything in images. 2025. 2, 3

[27] Tencent Hunyuan3D Team. Hunyuan3d 2.0: Scaling diffusion models for high resolution textured 3d assets generation, 2025. 3, 1

[28] Tencent Hunyuan3D Team. Hunyuan3d 2.5: Towards high-fidelity 3d assets generation with ultimate details, 2025. 1

[29] Bugra Tekin, Federica Bogo, and Marc Pollefeys. H+o: Unified egocentric recognition of 3d hand-object poses and interactions. In *Proceedings of the IEEE/CVF conference on computer vision and pattern recognition*, pages 4511–4520, 2019. 3

[30] Ruicheng Wang, Sicheng Xu, Cassie Dai, Jianfeng Xiang, Yu Deng, Xin Tong, and Jiaolong Yang. Moge: Unlocking accurate monocular geometry estimation for open-domain images with optimal training supervision. In *Proceedings of the Computer Vision and Pattern Recognition Conference*, pages 5261–5271, 2025. 4, 1

[31] Shibo Wang, Haonan He, Maria Parelli, Christoph Gebhardt, Zicong Fan, and Jie Song. Magichoi: Leveraging 3d priors for accurate hand-object reconstruction from short monocular video clips. In *Proceedings of the IEEE/CVF International Conference on Computer Vision*, pages 5957–5968, 2025. 2, 3, 7, 9, 10

[32] Bowen Wen, Wei Yang, Jan Kautz, and Stan Birchfield. Foundationpose: Unified 6d pose estimation and tracking of novel objects. In *Proceedings of the IEEE/CVF Conference on Computer Vision and Pattern Recognition*, pages 17868–17879, 2024. 4, 5, 1, 2

[33] Jiale Xu, Weihao Cheng, Yiming Gao, Xintao Wang, Shenghua Gao, and Ying Shan. Instantmesh: Efficient 3d

mesh generation from a single image with sparse-view large reconstruction models. *arXiv preprint arXiv:2404.07191*, 2024. 3

[34] Lixin Yang, Xinyu Zhan, Kailin Li, Wenqiang Xu, Jiefeng Li, and Cewu Lu. Cpf: Learning a contact potential field to model the hand-object interaction. In *Proceedings of the IEEE/CVF international conference on computer vision*, pages 11097–11106, 2021. 3

[35] Zhengdi Yu, Stefanos Zafeiriou, and Tolga Birdal. Dynhamr: Recovering 4d interacting hand motion from a dynamic camera. In *Proceedings of the Computer Vision and Pattern Recognition Conference*, pages 27716–27726, 2025. 3

[36] Jinglei Zhang, Jiankang Deng, Chao Ma, and Rolandos Alexandros Potamias. Hawor: World-space hand motion reconstruction from egocentric videos. In *Proceedings of the Computer Vision and Pattern Recognition Conference*, pages 1805–1815, 2025. 3

[37] Xiong Zhang, Qiang Li, Hong Mo, Wenbo Zhang, and Wen Zheng. End-to-end hand mesh recovery from a monocular rgb image. In *Proceedings of the IEEE/CVF international conference on computer vision*, pages 2354–2364, 2019. 3

[38] Yuxiao Zhou, Marc Habermann, Weipeng Xu, Ikhsanul Habibie, Christian Theobalt, and Feng Xu. Monocular real-time hand shape and motion capture using multi-modal data. In *Proceedings of the IEEE/CVF conference on computer vision and pattern recognition*, pages 5346–5355, 2020. 3

6. Implementation Details

Pipeline and dependencies. Our framework integrates several state-of-the-art foundation models. Crucially, we utilize **Gemini 3 Pro** [4] as the VLM agent responsible for keyframe selection and rigorous quality assessment. Guided by this agent, multi-view image synthesis is performed using the Gemini 2.5 Flash image generation model [4], while subsequent 3D mesh and texture generation are handled by Hunyuan 3D [27, 28]. For preprocessing, geometric priors including metric depth and segmentation masks are extracted via MoGe-2 [30] and SAM2 [21], respectively, with the initial object pose estimated by FoundationPose [32]. All differentiable rendering is implemented using PyTorch3D [20]. The entire pipeline, from preprocessing to optimization, is designed to run efficiently on a single NVIDIA 4090 GPU.

Online optimization strategy. Our method optimizes each frame sequentially via a two-stage alternating approach to ensure stability. Stage one optimizes hand translation (up to 200 iterations), followed by object 6D pose refinement (up to 400 iterations) with fixed hand parameters. exclusively for the onset frame, we optimize object scale by minimizing $\mathcal{L}_{\text{mask}}$ and the ray-traced contact loss $\mathcal{L}_{\text{contact}}$. During scale optimization, object rotation is fixed, and translation is constrained to the visual ray passing through the object center, thereby distinctively regularizing the solution space. Convergence is reached when the moving average of parameter variations, including scale when active, is less than 10^{-4} .

Optimizers and learning-rate schedule. For optimization, we employ separate Adam optimizers [11] for rotation and translation parameters. The object optimization uses fixed learning rates of 2×10^{-3} for rotation and 1×10^{-3} for translation. Similarly, hand optimization uses fixed learning rates of 1×10^{-3} for translation. We adopt constant learning rates throughout optimization, as we empirically observe that learning-rate decay does not lead to measurable accuracy improvements in our setting, while increasing the number of iterations required for convergence.

Loss terms and weights. The loss function employs the following weights: $\mathcal{L}_{\text{mask}}$ (L2) is weighted at 5.0, $\mathcal{L}_{\text{dino}}$ (L1) at 10.0. For physical interaction modeling, the ray-traced contact loss $\mathcal{L}_{\text{contact}}$ receives a weight of 5.0. Additionally, the relative position interaction loss $\mathcal{L}_{\text{interact}}$ is weighted at 400 for HO3D dataset and 200 for DexYCB dataset, with a maximum distance threshold of 0.05m to prevent spurious long-range attractions between hand and object. For the SDF based distance-weight gating function (Func.6), we set $\sigma = 40$.

Interaction Onset Frame selection. For HO3D, we identify the interaction onset as the earliest frame where the object exhibits significant motion while remaining fully visible. We quantify the motion by measuring the variation of the non-occluded object mask between consecutive frames:

$$r_i = \frac{\|(\mathcal{M}_o^{i+1} - \mathcal{M}_o^i) \odot (1 - \mathcal{M}_h^{i+1}) \odot (1 - \mathcal{M}_h^i)\|_1}{\|\mathcal{M}_o^i\|_1 + \varepsilon}, \quad (8)$$

where \mathcal{M}_o and \mathcal{M}_h denote the object and hand masks, respectively. The numerator captures the change in visible object pixels, while the denominator normalizes by the object area ($\varepsilon = 10^{-8}$ ensures stability). We select the first frame i that satisfies two criteria: (1) the motion ratio r_i exceeds a threshold $\tau = 0.025$, and (2) the object mask does not touch the image boundaries. The latter ensures the object is not truncated, thereby guaranteeing reliable geometric supervision.

7. Why Start at Interaction Onset?

We choose the interaction onset frame as the optimization anchor for two key reasons. First, metric scale alignment: since monocular object reconstruction suffers from scale ambiguity, the physical contact allows us to leverage the hand’s reliable metric scale to constrain and propagate the correct object size. Second, loss efficacy: the contact-based losses ($\mathcal{L}_{\text{contact}}$) are physically meaningful only when interaction occurs. Initiating optimization at this frame ensures these geometric constraints provide valid gradients for precise hand–object alignment.

8. Sequence Used

We evaluate our method on sequences from the DexYCB [2] and HO3D [8] datasets. Specifically, as shown in Table 3 and Table 4, we randomly select 18 sequences from HO3D and 20 sequences from DexYCB, covering a diverse range of object types and hand-object interaction patterns. For the HO3D dataset, we begin processing from the identified IOF to ensure meaningful interaction modeling. HO3D sequences vary in length from 800 to 1600 frames; for computational efficiency, we cap the processing at 1024 frames per sequence. For the DexYCB dataset, each selected sequence spans approximately 80 frames. Unless otherwise specified, we uniformly subsample all sequences with a stride of 5 (i.e., processing every fifth frame), which balances temporal coverage with computational cost. These sequences are chosen to provide comprehensive coverage of common manipulation scenarios and object categories, enabling robust evaluation of our method’s generalization capabilities across different interaction types and geometric configurations.

Table 3. Sequences selected from the HO3D datasets.

Sequence ID	Object	IOF Index
ABF12	bleach cleanser	100
ABF14	bleach cleanser	100
BB12	banana	200
BB13	banana	130
GPMF12	potted meat	105
GPMF14	potted meat	100
GSF13	scissors	100
GSF14	scissors	80
MC1	cracker box	0
MC4	cracker box	0
MDF12	power drill	150
MDF14	power drill	250
ShSu10	sugar box	50
ShSu12	sugar box	110
SM2	mustard	0
SM4	mustard	0
SMu1	mug	20
SMu40	mug	0

Table 4. Sequences selected from the DexYCB datasets.

Sequence ID	Object
20200709-subject-01/20200709_141754/836212060125	master chef can
20200709-subject-01/20200709_142853/836212060125	master chef can
20200813-subject-02/20200813_154204/836212060125	bleach cleanser
20200813-subject-02/20200813_153453/836212060125	power drill
20200820-subject-03/20200820_141856/836212060125	potted meat
20200820-subject-03/20200820_143330/836212060125	mug
20200903-subject-04/20200903_103554/836212060125	master chef can
20200903-subject-04/20200903_113012/836212060125	wood block
20200908-subject-05/20200908_144138/836212060125	tomato soup can
20200908-subject-05/20200908_152416/836212060125	large clamp
20200918-subject-06/20200918_113441/836212060125	sugar box
20200918-subject-06/20200918_114747/836212060125	potted meat
20200928-subject-07/20200928_153800/836212060125	pitcher base
20200928-subject-07/20200928_144300/836212060125	mustard bottle
20201002-subject-08/20201002_110940/836212060125	pitcher base
20201002-subject-08/20201002_105558/836212060125	mustard bottle
20201015-subject-09/20201015_143700/836212060125	mustard bottle
20201015-subject-09/20201015_142940/836212060125	cracker box
20201022-subject-10/20201022_111745/836212060125	mustard bottle
20201022-subject-10/20201022_111209/836212060125	sugar box

9. Analysis on Results of Baselines

On the DexYCB dataset, both baselines exhibited varying degrees of failure. Specifically, HOLD encountered issues in some sequences where it failed to obtain the hand/object mesh due to inaccurate poses, which prevented the geometric structure from being effectively learned. Meanwhile, MagicHOI was unable to complete colmap reconstruction in most sequences and thus could not obtain stable poses for subsequent processing. On the other hand, MagicHOI’s hand-object alignment relies on the geometry generated by its generative model. Due to the limitations of its capabilities, it fails to produce reasonable geometric structures in some challenging cases, leading to the failure of the final

results.

10. Impact of texture refinement on pose initialization.

As shown in Table 5, texture quality plays a decisive role in the performance of the subsequent pose estimation. FoundationPose [32] adopts an analysis-by-synthesis approach, estimating the 6D pose by comparing the similarity between the input image and renderings of the object mesh. Consequently, accurate appearance modeling is critical for minimizing the domain gap between synthesized and observed views. Relying solely on the initial coarse texture leads to significant appearance discrepancies, which confuse the scoring network and result in a high mean rotation error of 118.41° . In contrast, our texture refinement recovers high-fidelity surface details that closely match the visual observation. This photorealism enables FoundationPose to compute more reliable similarity scores, drastically reducing the rotation error to 81.55° and improving the ADDS accuracy from 18.52% to 27.42%. These results validate that precise texture recovery is not merely a visual enhancement but a prerequisite for robust geometry-based pose estimation.

11. Comparison with Generative 3D Initialization

Table 6 presents a comparative analysis against SAM3D [26], a state-of-the-art method that jointly estimates shape and pose from a single image.

Experimental Setup. Given that SAM3D operates on a single-frame basis, we evaluate it on every 5th frame across all 18 scenes in the HO3D dataset. Conversely, our method generates a single canonical mesh using VLM-guided multi-view synthesis and estimates the pose for each frame using FoundationPose initialized with MoGe-2 metric depth.

Analysis. The fundamental limitation of SAM3D lies in *geometric hallucination* due to occlusion. As a single-view model, it is forced to reconstruct unobserved regions based on learned priors rather than temporal evidence. This often leads to geometries that are topologically plausible but inconsistent with the ground truth, as evidenced by the high Chamfer Distance (1.35 vs. 0.27 cm^2). Such geometric inconsistency inherently compromises pose estimation accuracy, as the predicted pose lacks a faithful 3D reference to align with the input image, resulting in a large rotation error of 118.71° . In contrast, by aggregating multi-view cues, our approach maintains rigorous geometric consistency, enabling reliable, metric-scale pose estimation even under heavy occlusion. A qualitative comparison of the reconstructed geometry is illustrated in Figure 9.

Table 5. **Impact of Texture Refinement on FoundationPose Initialization.** We compare the pose estimation performance on the HO3D dataset using the original coarse texture (w/o Refinement) versus our refined texture (w/ Refinement). FoundationPose yields significantly lower rotation errors and higher accuracy scores when supplied with the refined, photorealistic texture.

Method	R Err. (°)↓	T Err. (mm)↓	ADD (%)↑	ADDs (%)↑	MSSD↑	MSPD↑	VSD↑	AR↑
w/o Refinement (Coarse Texture)	118.41	10.37	0.42	18.52	5.70	2.93	2.86	3.83
w/ Refinement (Ours)	81.55	10.35	6.36	27.42	19.09	7.25	5.28	10.54

Table 6. **Comparison with Generative 3D Baseline (SAM3D).** Quantitative comparison of pose initialization and geometric fidelity against the single-view baseline SAM3D. Our initialization approach significantly reduces geometric error and improves pose alignment across all metrics.

Method	R Err.° ↓	T Err. (mm)↓	CD (cm ²)↓	F@5 (%)↑	F@10 (%)↑	ADDs (%)↑	MSSD↑	MSPD↑	VSD↑	AR↑
SAM3D	118.71	24.85	1.35	67.01	87.44	9.06	0.80	0.00	5.62	2.47
Our Initialization	81.55	10.35	0.27	86.63	97.77	27.42	19.09	7.25	5.28	10.54

Table 7. Comparison of computational cost. Our method requires significantly less preprocessing and runtime than existing methods.

Method	Preprocessing Time	Runtime
HOLD	~2 h	>24 h
MagicHOI	~2 h	~2 h
Ours	~15 min	~1.5 h



Figure 9. Qualitative comparison with SAM3D [26]. Our method significantly outperforms SAM3D in terms of both geometry and texture.

12. Computation Cost

Our optimization process is computationally efficient. On a single NVIDIA RTX 4090 GPU, each frame requires approximately 30–50 seconds for optimization. Unless otherwise specified, we process every fifth frame of each sequence. As a result, the total computation time scales linearly with the sequence length. On average, a sequence of 1000 frames (200 frames after downsampling) can be processed in approximately 1.5 hours, which is consistent with the overall runtime reported in Table 7.

13. Details of VLM-Guided 3D Generation

In this section, we provide the detailed prompt specifications and evaluation protocols used in our agentic generation pipeline. Our framework leverages a Vision-Language Model (VLM) as an intelligent supervisor to guide three critical stages: (1) informative keyframe selection, (2) consistent multi-view synthesis, and (3) high-fidelity texture refinement. For each stage, we present the system instructions, task definitions, and representative VLM responses. The prompts presented below are the exact instructions used in our pipeline to ensure reproducibility.

13.1. Stage 1: Informative Keyframe Selection

The objective of this stage is to filter the input video stream and identify a minimal set of frames that maximize geometric coverage while minimizing occlusion.

13.1.1. Prompt Specification

```

1  {
2      "system_role": "You are an expert
       in computer vision,
       specializing in selecting
       frames that best showcase the

```

```

    complete appearance of an
    object from multiple images.",

3  "task": "Select {num_frames}
    images from the following
    candidate frames. The selected
    images must:
4  1. Clearly display different
    angles of the object.
5  2. Maximize coverage of the
    object's complete appearance
    (front, back, left, right, top,
    bottom).
6  3. Be sharp, with the object fully
    visible and minimal occlusion.
7  4. Have the maximum possible
    viewpoint difference between
    selected frames.
8  5. Feature the object occupying a
    relatively large portion of the
    frame.",
9  "response_format": "
10 {
11   "selected_frames": [1, 5, 10,
12     15], // Indices of selected
13     frames
14   "reasoning": "Reason for
15     selection",
16   "coverage": {
17     "front": true,
18     "back": true,
19     "left": true,
20     "right": false
21   }
22 }
23 "instruction": "Please reply
    strictly in JSON format without
    adding other explanatory text."

```

Listing 1. Prompt for Keyframe Selection

13.1.2. Example Response

```

1  {
2   "selected_frames": [1, 5, 13, 21],
3   "reasoning": "Frame 1 is selected
    as the standard front view,
    clearly displaying the main
    brand label. Frame 5 shows the
    back of the object, clearly
    presenting the ingredients list
    and nutritional information.

```

Frame 13 provides the side profile, effectively showcasing the object's depth, thickness, and side curves. Frame 21 captures the bottom perspective, supplementing this often-overlooked angle. All four images are high-definition, have a large object-to-frame ratio, and exhibit significant viewpoint differences, achieving maximum multi-angle coverage.",

```

4  "coverage": {
5    "front": true,
6    "back": true,
7    "left": true,
8    "right": false,
9    "top": false,
10   "bottom": true
11 }
12 }

```

Listing 2. VLM Response for Keyframe Selection

13.2. Stage 2: Multi-View Synthesis and Validation

Based on the selected keyframes, we generate four orthogonal views. To ensure consistency, a VLM critic evaluates the generated views against strict geometric and texture criteria.

13.2.1. Generation Prompts

```

1  {
2   "multiview_generation": {
3     "static_object": "Generate a
        complete image of the water
        bottle in the picture from four
        perspectives: front, back,
        left, and right. Require
        photorealism. Present as a
        four-view grid. Remove the
        plate and extraneous objects.
        Pure white background. The
        image must not contain text
        indicating viewpoint direction
        (e.g., front, back, left,
        right).",
4     "hand-held_object": "Generate a
        complete image of the object
        held in the hand from four
        perspectives: front, back,

```

```

13    left, and right. Require
14    photorealism. Present as a
15    four-view grid. Remove the hand
16    and hallucinate/complete the
17    regions occluded by the hand.
18    Pure white background. The
19    image must not contain text
20    indicating viewpoint direction.
21    The object size should be
22    consistent across all four
23    views."
24
25    }
26  }

```

Listing 3. Prompts for Multi-View Generation

13.2.2. Validation Protocol (The "Critic")

```

1  {
2    "validation": {
3      "system_role": "You are an expert
4        in 3D modeling, material
5        analysis, and multi-view image
6        quality assessment. Please
7        carefully analyze the following
8        images:",
9      "task_description": "Task:
10        1. The first image(s) are the
11          original input, showing the
12          appearance, texture, and
13          material of an object.
14        2. The last image is the
15          generated 'four-view' image,
16          which should display the
17          complete image of the object
18          from four different
19          perspectives (front, back,
20          left, right) while preserving
21          the original visual
22          attributes.",
23      "evaluation_criteria": "Criteria:
24        Level 1: Veto Items
25        1. Text Check: Does the generated
          image contain any text, labels,
          or viewpoint descriptions
          (e.g., front, back)? If yes,
          terminate evaluation; result is
          invalid.
26
27        Level 2: Core Dimension Scoring
28          (0-10)

```

```

13    2. Geometry & View Correctness
14      (Weight: 30%): Are viewpoints
15      correct? Is orientation
16      consistent (no rotation)? Any
17      rotation results in large
18      deductions.
19    3. Texture & Material Fidelity
20      (Weight: 20%): Are surface
21      textures (e.g., patterns) and
22      material properties (e.g.,
23      reflection) consistent with the
24      original?
25    4. Geometric Detail Integrity
26      (Weight: 20%): Are key
27      geometric details (chamfers,
28      holes, embossing) preserved?
29    5. Feature Consistency (Weight:
30      15%): Is it the same object in
31      terms of shape, style, and
32      color?
33    6. Image Quality (Weight: 15%):
34      Is the image clear, noise-free,
35      and on a pure white background?
36
37    Level 3: Deductions
38    - Rotated views: -3 points each.
39    - Poor layout: -1 to -2 points.",
40    "response_format": "JSON format
41      containing: is_valid,
42      score_overall, score_breakdown,
43      has_text, rotated_views,
44      improvement_suggestions,
45      summary_feedback, etc.",
46    "instruction": "Reply strictly in
47      JSON. First check veto items."
48  }
49 }

```

Listing 4. Prompt for Multi-View Validation

13.3. Stage 3: Texture Refinement and Agentic Editing

After lifting the multi-view images to 3D and unwrapping UVs, we perform a texture refinement step. A VLM critic detects artifacts (e.g., hallucinated content, missing details) and guides a subsequent editing pass.

13.3.1. Texture Validation Protocol

```

1  {
2    "texture_validate": {

```

```

3   "system_role": "You are an expert
4   in 3D texture mapping analysis,
5   material comparison, and image
6   consistency assessment.
7   Carefully analyze the images.",
8   "task_description": "Task:
9   1. Image 1: The four-view image.
10  2. Image 2: The generated Texture
11  Map.
12  3. Evaluate if the texture map
13  accurately reproduces all
14  texture information from the
15  four-view image, focusing on
16  completeness, fictional
17  content, and correspondence.",
18  "evaluation_criteria": "Criteria:
19
20  Level 1: Veto Items
21  - Invalid texture map (blank,
22  pure color, severe distortion).
23  - Key features completely missing.
24
25  Level 2: Core Dimensions
26  2. Completeness (Weight: 30%):
27  Are all visible textures
28  present? (Deduction: -2 per
29  major missing item).
30  3. Accuracy/No Fiction (Weight:
31  25%): Does it contain
32  hallucinated content not
33  present in the source? (Severe
34  penalty: -3 to -5 points).
35  4. Correspondence (Weight: 20%):
36  Are textures mapped to correct
37  UV islands?
38  5. Color/Material (Weight: 15%):
39  Consistency in color, shading,
40  and saturation.
41  6. Fidelity (Weight: 10%):
42  Resolution and detail
43  preservation.
44
45  Level 3: Extra Deductions
46  - Seams, repetitions,
47  stretching.",
48  "response_format": "JSON format
49  containing: is_valid,
50  score_overall,
51  fictional_content_analysis,
52  missing_content_analysis,
53  texture_coverage_analysis,
54  etc.",

```

```

24  "instruction": "Strictly follow
25  JSON format. Pay special
26  attention to 'fictional
27  content', any texture appearing
28  in the map but not in the
29  source views is a severe error!"
30  }
31  }

```

Listing 5. Prompt for Texture Map Validation

13.3.2. Example Validation Result (Invalid Case Detected)

```

1  {
2  "is_valid": false,
3  "score_overall": 0.0,
4  "fictional_content_analysis": {
5  "has_fictional_content": true,
6  "fictional_items": [
7  {
8  "type": "severe",
9  "description": "The entire back
10 texture is a fabricated copy of
11 the front label instead of the
12 nutrition facts panel shown in
13 the source.",
14 "location_in_texture": "The
15 second large body island in the
16 texture map.",
17 "deduction": 5
18 }
19 ],
20 "total_fictional_deduction": 5
21 },
22 "summary_feedback": "Invalid.
23 Critical error: the back side
24 texture is a fabrication (copy
25 of the front). This makes the
26 model unusable for pose
27 estimation from rear
28 viewpoints."
29 }

```

Listing 6. Example Validation Result detecting hallucinations

13.3.3. Refinement Prompt Construction

Based on the negative feedback from the validation step, we programmatically construct a structured refinement command to guide the image-to-image editing model.

```
1  {
2    "texture_refinement_task": {
3      "base_instruction": "Below are
4        object images from multiple
5        views and their texture map.
6        Please edit the texture map
7        based on the following
8        critique:",
9      "injected_feedback": "Invalid.
10        Critical error: the back side
11        texture is a fabrication (copy
12        of the front). This makes the
13        model unusable for pose
14        estimation from rear
15        viewpoints.",
16      "geometric_constraints": "Do not
17        change the layout or shape of
18        UV islands. Only align the
19        content with reference images.
20        The bottom-left area
21        corresponds to the bottom
22        view.",
23      "specific_corrections": "Change
24        the purple/black artifact
25        regions to match the red color
26        of other parts. Adjust tone for
27        vibrancy. Fix text and
28        patterns."
29    }
30 }
```

Listing 7. Structured Input for Texture Refinement